Tunable Spectral Ordering of Magnetic Plasmon Resonances

Nicholas P. Montoni, Steven C. Quillin, Charles Cherqui, and David J. Maisello*

Department of Chemistry, University of Washington, Seattle, WA 98195

E-mail: masiello@chem.washington.edu

Abstract

Abstract.

Keywords

magnetic plasmons, plasmon metamolecules

Clusters of metal nanoparticles (MNPs) that exhibit anomalously strong magnetic fields, called plasmon oligomers or plasmon metamolecules, have been of great interest in recent years.[1–6] Magnetic plasmon resonances in these systems have been shown to couple to and enhance the magnetic field of light and hybridize analogously to electric plasmon resonances.[7–13] The magnetic properties of single oligomers, i.e. those systems composed of only one ring of MNPs, are now well understood based upon models in the quasistatic limit.[4,6,14,15] Conversely, the infinite-oligomer regime has also been understood within the language of tight-binding models of solid-state physics.[16,17] Recently, a disconnect between these size regimes and methods has arisen, leading to open questions in how magnetic plasmon resonances behave in few-oligomer assemblies, called the intermediate size regime.[9–13]

Most crucial to this disconnect is the question of when and how retardation effects matter. For example, in the case of the two oligomer cluster (the 2-mer) the quasistatic approximation has been shown to deviate from full-wave numerical electrodynamics simulations in that it predicts a different energy-ordering of the magnetic plasmon resonances.[11] Retardation effects have been incorporated into models of single MNPs,[18] dimers,[19,20] and infinite chains and arrays.[16,21–31] However, with the exception of numerical studies, no analytical models include retardation effects in the description of magnetic plasmon oligomers. Here, we show that the incorporation of retardation effects corrects the aforementioned discrepancy between model and simulation, and further points to the facile ability to tune the magnetic plasmon spectrum via scaling oligomer size. This is important because it allows for the facile manipulation of the effective permittivity and permeability thereby facilitating the design of future tunable optical metamaterials.

In the following, we demonstrate the evolution of the magnetic plasmon resonances in intermediate-size N-mers with size by including the full field within a coupled dipole approach describing their interaction. Interestingly, as a function of size, the magnetic resonances switch their ordering in analogy to the way that electric plasmon resonances in hybridized nanoparticles can switch order.[20] We further analyze the distinct radiative properties of each magnetic plasmon resonance by computing the angle-resolved cathodoluminescence (CL) spectrum.[32–35] The spectral ordering depends not only on aggregate size but also upon oligomer morphology which we examine below. The ability to choose the resonance frequency of specific magnetic plasmon resonances will lead to advances in superlensing and electromagnetic cloaking at optical frequencies, as these applications stem directly from tunable negative-index metamaterials.[36–42]
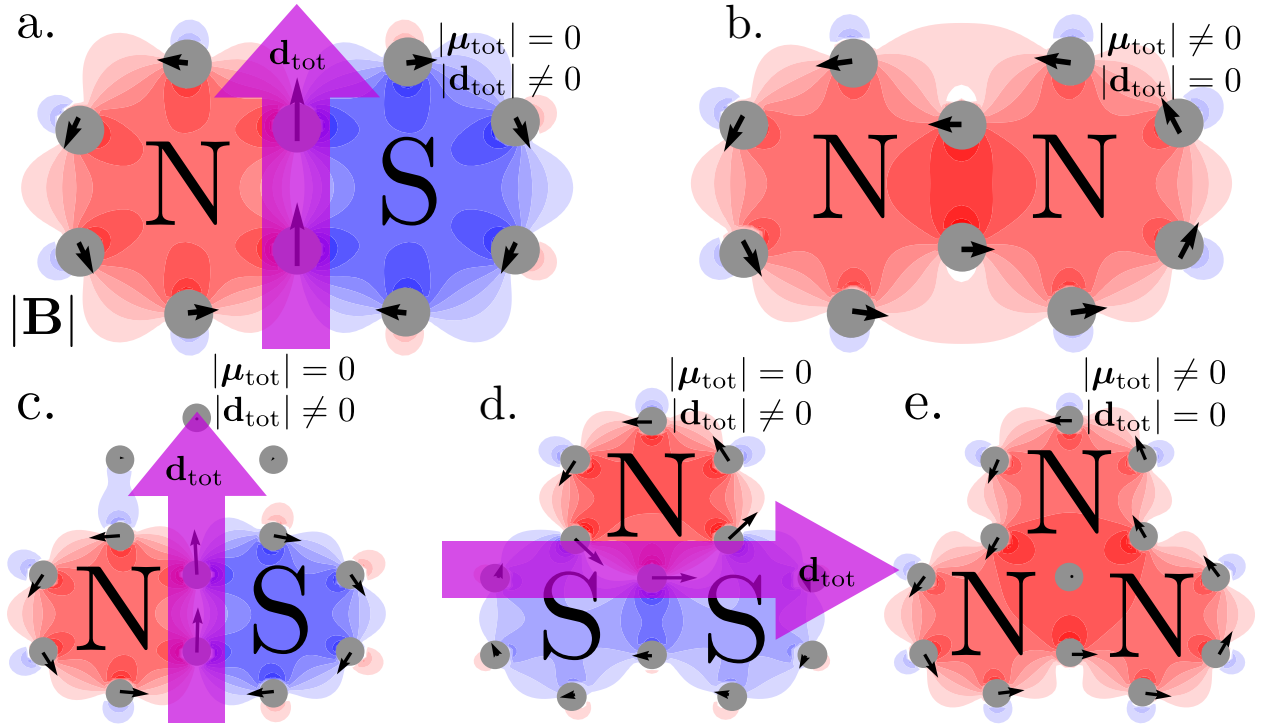
Figure 1: Magnetic field plots of the 2mer (a and b) and 3mer (c, d, and e) oligomers. Each system supports a number of closed-loop magnetic plasmon resonances equal to the number of rings in the system. The magnetic plasmons support an electric dipole moment (a, c, and d) support out-of-phase magnetic fields. The nodeless magnetic modes (b and e) support a net magnetic dipole moment are accessible to the magnetic field of light.

1 Model Theory

Figure 1 displays two model systems, the 2-mer and 3-mer, comprising 10 and 13 silver nanospheres in analogy to naphthalene and phenalene. The mapping of the electric localized surface plasmon resonances of individual noble metal nanoparticles onto harmonic oscillators is now well-understood.[43] In the limit where each nanoparticle, here restricted to a spherical geometry of radius a, possesses only an electric dipole plasmon resonance, the equations of motion dictating the electromagnetic response of the oligomer are

$$\ddot{\mathbf{q}}_i = -\omega_{\mathrm{sp}}^2 \mathbf{q}_i + \frac{e}{m_{\mathrm{sp}}} \sum_{i,j \neq i} \mathbf{E}_j(\mathbf{r}_i), \tag{1}$$

where ω_{sp} is the natural frequency of the Mie resonance, $m_{\mathrm{sp}} = e^2/\alpha_{\mathrm{sp}}\omega_{\mathrm{sp}}^2$ is the plasmon's effective mass defined in terms of the polarizability $\alpha_{\mathrm{sp}} = 3a^3/(\varepsilon_\infty + 2\varepsilon_b)$, with ε_∞ and ε_b the high-frequency and background dielectric functions. The dipole moment of each plasmon oscillator, restricted to lie in the plane of the oligomer at position $\mathbf{r}_i$, is $\mathbf{d}_i = e\mathbf{q}_i$ and $\mathbf{E}_j(\mathbf{r}_i)$ is the fully retarded electric field of the jth dipole evaluated at the position of the ith dipole. The electric field is defined by

$$\mathbf{E}_j(\mathbf{r}_i) = \mathbf{\Lambda}_{ij} \cdot \mathbf{d}_j = \left\{ \left(\frac{1}{r_{ij}^3} - \frac{ik}{r_{ij}^2} \right) (3\hat{\mathbf{n}}_{ij}\hat{\mathbf{n}}_{ij} - \mathbf{1}) - \frac{k^2}{r_{ij}} (\hat{\mathbf{n}}_{ij}\hat{\mathbf{n}}_{ij} - \mathbf{1}) \right\} \frac{e^{ikr_{ij}}}{\varepsilon_b} \cdot \mathbf{d}_j, \tag{2}$$

where, $\hat{\mathbf{n}}_{ij}$ is the unit vector connecting two dipoles separated by distance r_{ij}, $k = \sqrt{\varepsilon_b}\omega/c$ where ω is the oscillatory frequency of the jth dipole. Interestingly, the far-field term carries the opposite sign of the near-field term. The field is decomposed into three parts: the near- (r_{ij}^{-3}), intermediate- (r_{ij}^{-2}), and far-field (r_{ij}^{-1}). All dipolar retardation effects are included in this field.[44] Due to the relative magnitudes of these terms and the sign of $e^{ikr_{ij}}$ the interaction energies can change sign and go from energy-lowering to energy-raising.

As described in the methods section, there are as many normal modes of each N-mer as

there are electric dipole plasmons. Of these normal modes, some are electric in character and some are magnetic in character with N magnetic plasmon resonances for each N-mer studied here. Figure 1 shows these magnetic plasmon normal modes overlaid with their associated signed magnetic field magnitude. Each mode is named for its particular magnetic field distribution after the poles of a magnet, either all-North (aN) or North-South (NS). The top right-hand corner of each panel indicates whether the mode depicted has a net electric dipole or a net magnetic dipole moment. In planar geometries, the magnetic dipole moments are always perpendicular to the in-plane electric dipole moments. As a result, they scatter light with different directionality as will be discussed.

2   Spectral Ordering of Magnetic Modes in Model Systems

To determine the impact of incorporating retardation effects, it is first useful to consider the quasistatic limit. Here individual particle frequencies (define omegasp) are size independent and the coupling strength depends only upon the scale $s = r_{ij}/a$ and not upon the overall oligomer size. That is, if this ratio s of inter-particle distance r_{ij} to particle size a remains constant, as the particles grow the collective frequencies do not change. This is evident by considering the k goes to zero limit of the electric field in Equation 2,

$$
\begin{aligned}
\lim_{k \to 0} \mathbf{E}_j(\mathbf{r}_i) &= \frac{e^2}{m_{\mathrm{sp}}} \mathbf{\Lambda}_{ij} \\
&= \frac{\omega_{\mathrm{sp}}^2 \alpha_{\mathrm{sp}}^2}{\varepsilon_b} \frac{3\hat{\mathbf{n}}_{ij}\hat{\mathbf{n}}_{ij} - \mathbf{1}}{r_{ij}^3} \cdot \mathbf{d}_j \\
&= \frac{\omega_{\mathrm{sp}}^2}{\varepsilon_b} \left(\frac{3}{\varepsilon_\infty + 2\varepsilon_b} \right) \frac{3\hat{\mathbf{n}}_{ij}\hat{\mathbf{n}}_{ij} - \mathbf{1}}{s^3} \cdot \mathbf{d}_j
\end{aligned}
\tag{3}
$$

where m_{sp} and α_{sp} are rewritten in terms of fundamental parameters for silver: $\varepsilon_\infty = 3.77$, $\hbar\gamma = 0.05$ eV, and $\hbar\omega_p = 9.1$ eV. Retardation effects, however, remove this invariance and introduce size-dependence into both the individual plasmon natural frequency as well as into

the electric field. Consequently, in the following we choose the individual MNP radius a as the independent variable, fixing the nearest neighbor distance at $3a$, to investigate the effects of retardation upon the magnetic plasmon spectrum in intermediate-size N-mers.

Figure 2 shows the predicted resonance energies from both the model and full-wave optical simulations of the 2-mer and 3-mer with increasing a.[45] At small sizes the magnetic modes preserve the quasistatic ordering predicted in previous work, which is to be expected when the oligomer system fits within a wavelength of light and the near-field dominates the electric field.[11] As the system size increases, the resonance energies decrease and to cross at $a = 7$ nm, and once more at $a = 20$ nm. This is due to the far-field contribution in Equation 2 becoming large relative to the near- and intermediate-fields, as shown in Figure 2b and d (squares). The second crossing of the eigenmodes recovers the ordering at small sizes, which might lead to the erroneous conclusion that the quasistatic approximation is accurate again. Rather, both eigenmode crossings are due entirely to retardation effects. The interaction energy between all the dipoles in each magnetic mode, [reformat equation]

$$U_{\text{int}} = -\frac{1}{2} \sum_{ij} \mathbf{d}_i \cdot \mathbf{E}_j(\mathbf{r}_i), \tag{4}$$

with the same $\mathbf{E}_j$ defined in Equation 2, explains why the modes cross at certain system sizes. The inclusion of the far-field, the third term in Equation 2 is the cause of the mode switching, as it carries the opposite sign of the near- and intermediate-field terms. These terms with opposite splitting are the cause of the mode crossings; as the near- and intermediate-fields lower the energy of the North-South mode, the far-field raises the energy of the North-South mode, and vice-versa for the North-North mode. Close inspection of Figure 2b reveals that the crossing points occur where the splitting in the near- and intermediate-fields is equal and opposite to that of the far-field. Perhaps more interestingly, in any dielectric medium with $\varepsilon_b > 1$ the crossing points are shifted towards smaller scale due to wavelength contraction. This can also be explained through the impact of a dielectric medium on coupling strength. While a medium should contribute an overall increase to the coupling strength, the far-field
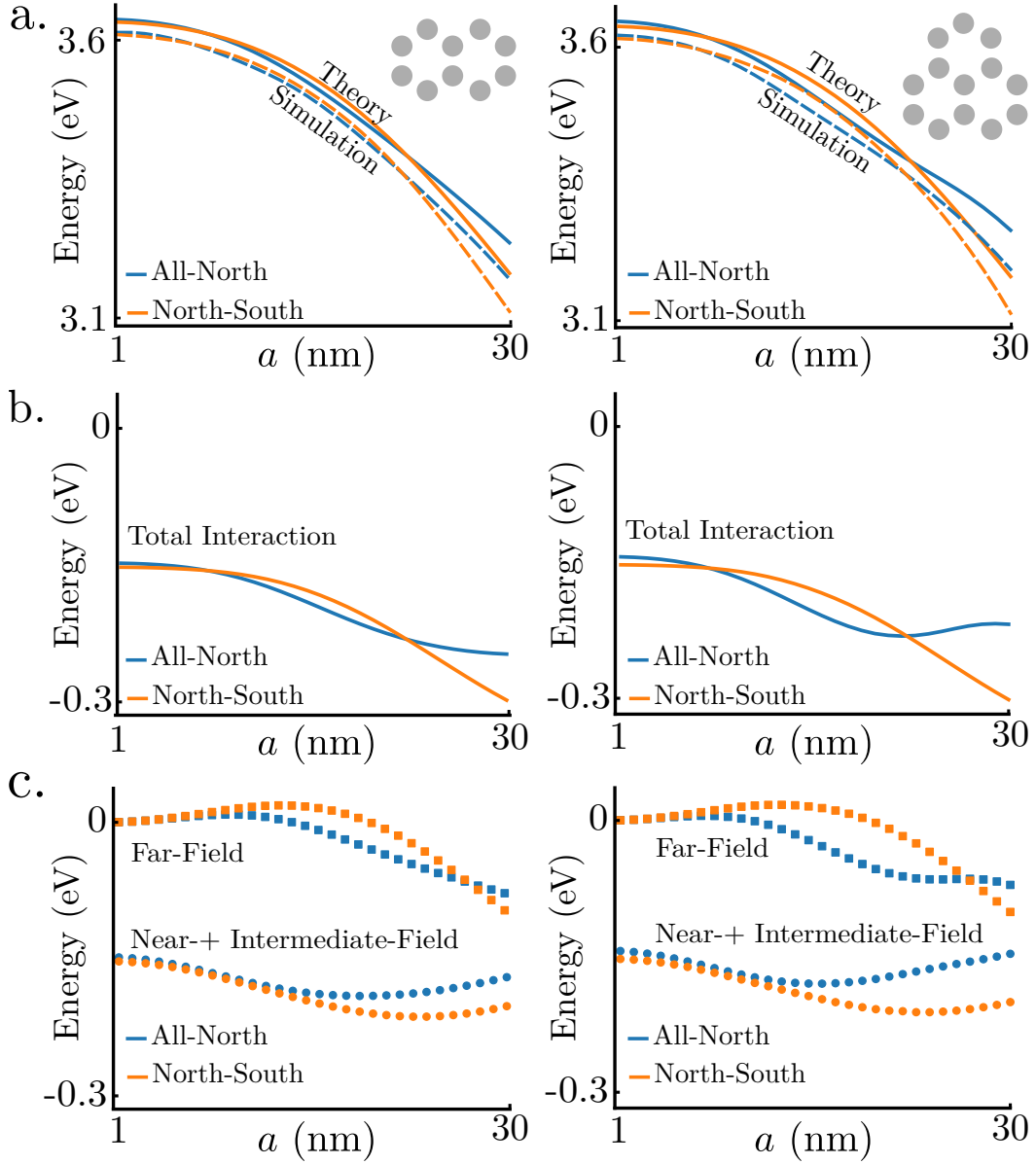
Figure 2: Eigenenergies (a and c) and interaction energies (b and d) for the 2mer and 3mer. At small scales $r_0 < 5$ nm the magnetic modes are ordered as predicted using a quasistatic model, with NS (orange) lower in energy than aN (blue). This implies that for very small oligomer systems, the quasistatic approximation is still accurate. However, at sizes greater than $r_0 = 5$ nm and smaller than $r_0 = 20$ nm, the eigenmodes switch order. This is due to the dominance of the far-field term, which is evident from (b and d). Finally, at sizes greater than $r_0 = 20$ nm, the eigenmodes switch order again. Also plotted are simulated peak positions of each mode (dashed lines) to show agreement within 0.1 eV.

term should be more drastically impacted due to its extra ε_b-dependence through its k^2 term.[46]

Previous work has explored the oscillatory nature of hybridized electric dipole plasmon resonance frequencies and radiation damping as a function of separation in noble metal dimers.[20] Analogously, our work shows that magnetic plasmon resonance energies also oscillate with interparticle separation and can be understood via analysis of the contributions to the dipole-dipole interaction.

3 Radiative Properties of Magnetic Plasmon Resonances

Only those magnetic resonances supporting net electric or magnetic dipole moments will radiate to the far field. The magnetic dipole moment of the aN magnetic mode is perpendicular to the electric dipole moment(s) of the NS mode in both the model 2-mer and 3-mer. This means that these modes radiate with different directionality. It has been predicted and shown experimentally that 1-mers scatter light anisotropically when both their magnetic dipole moment and electric dipole moment are mutually excited,[4,12] as is evident in differential scattering spectra and profiles. Both observations stem from the differential power,[47,48]

$$\frac{dP}{d\Omega} = \frac{c}{8\pi}\text{Re}\left[r^2\hat{\mathbf{n}} \cdot \sum_i \mathbf{E}_i \times \sum_j \mathbf{B}_j^*\right] \tag{5}$$

$\mathbf{E}_i$ and $\mathbf{B}_i$ are produced from the sum of effective electric ($\mathbf{d}_i$) and magnetic ($\boldsymbol{\mu}_i$) dipole moments of each ring of the N-mer, assumed to be co-located at the center of the i-th ring and oscilalting in time as $e^{-\mathrm{i}\omega t}$. In this approxiamtion, the differential power becomes[1]

$$\frac{dP}{d\Omega} = \frac{ck^4}{8\pi}\text{Re}\left\{\hat{\mathbf{n}}\cdot\left[\left(\sum_i(\hat{\mathbf{n}}\times\mathbf{d}_i)\times\hat{\mathbf{n}} - \hat{\mathbf{n}}\times\boldsymbol{\mu}_i\right)\times\left(\sum_j\hat{\mathbf{n}}\times\mathbf{d}_j^* + (\hat{\mathbf{n}}\times\boldsymbol{\mu}_j^*)\times\hat{\mathbf{n}}\right)\right]\right\}$$

$$= \frac{ck^4}{8\pi}\text{Re}\left[\sum_{ij}\mathbf{d}_i\cdot\mathbf{d}_j^* - (\hat{\mathbf{n}}\cdot\mathbf{d}_i)(\hat{\mathbf{n}}\cdot\mathbf{d}_j^*) + \boldsymbol{\mu}_i\cdot\boldsymbol{\mu}_j^* - (\hat{\mathbf{n}}\cdot\boldsymbol{\mu}_i)(\hat{\mathbf{n}}\cdot\boldsymbol{\mu}_j^*)\right. \tag{6}$$

$$\left. + \hat{\mathbf{n}}\cdot(\mathbf{d}_i\times\boldsymbol{\mu}_j^* + \mathbf{d}_j^*\times\boldsymbol{\mu}_i)\right].$$

Notice that the first two terms are due to electric and magnetic dipole radiation, while the third term is due to their interference. To build intuition, we demand the magnetic dipole $\boldsymbol{\mu}$ is oriented in the z-direction, and the electric dipole $\mathbf{d}$ is oriented in the y-direction. The coarse-grained electric dipole and magnetic dipole can be written in terms of their constituent dipoles $\mathbf{d} = \sum_n d_{e,n}\hat{\mathbf{y}}$ and $\boldsymbol{\mu} = \frac{k}{2}\sum_n(\mathbf{r}_n\times d_{m,n}\hat{\boldsymbol{\phi}}_n) = \frac{kNRd_m}{2}\hat{\mathbf{z}}$ where the sums are taken over the n-th and m-th dipoles, respectively.

Figure 3 displays the differential power profiles associated with the aN and NS magnetic plasmon resonances, as well as the interference pattern, of any N-mer. Since the aN mode has only a z-oriented magnetic dipole, its radiation pattern is orthogonally oriented with respect to that of the y-directed electric dipole of the NS mode. Thus, examination of the directionality of radiation allows one to determine the net electric or magnetic dipole character. Strong forward/backward scattering asymmetries are also predicted and demonstrated in metal-semiconductor core-shell nanoparticle assemblies, which similarly exploit the interference between electric and magnetic plasmons.[49]

4 Angle-Resolved Cathodoluminescence for Observing Spectral Switching

Recent studies have demonstrated the utility of angle-resolved CL spectroscopy to characterize plasmon resonances in noble metal nanoparticles.[33–35,43,50] Using an electron microscope

a.

z

y

NS mode

b.

z

y
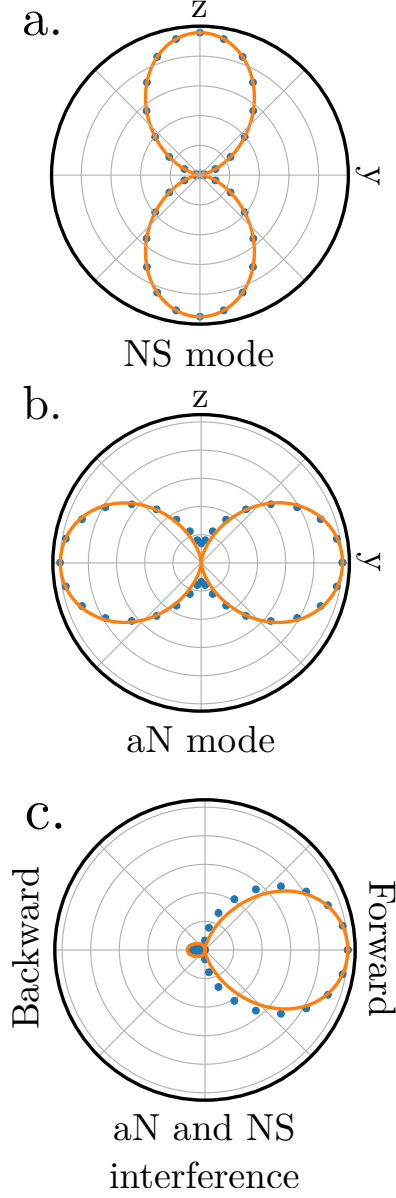
aN mode

c.

Backward

Forward

aN and NS
interference

Figure 3: Magnetic field distributions of a magnetic dipole mode (a) and an electric dipole mode (c) in the xy-plane with corresponding radiation patterns (b and d) in the yz-plane. The magnetic dipole exhibits the expected dipolar doughnut, or two lobe, shape with a node along the z-axis. The electric dipole moment also shows the expected pattern with a node along the y-axis.

fitted with a parabolic mirror, emitted CL radiation can be collected across a large portion of the backward scattering hemisphere.[33–35] Here we show that with the selection rules imposed by the location of the electron beam and the specific directionality of the emission from each magnetic mode, the magnetic modes of the N-mers and their crossings can be observed in angle-resolved CL spectra. The previous section built up intuition regarding the directionality of light scattered by the magnetic modes of the 2-mer and 3-mer. This intuition informs the particular angles at which to collect CL spectra associated with each magnetic mode. More specifically, based upon the selection rules imposed by the electron beam and the directionality of CL radiation, it is possible to distinguish the magnetic modes and their spectral ordering as a function of size.
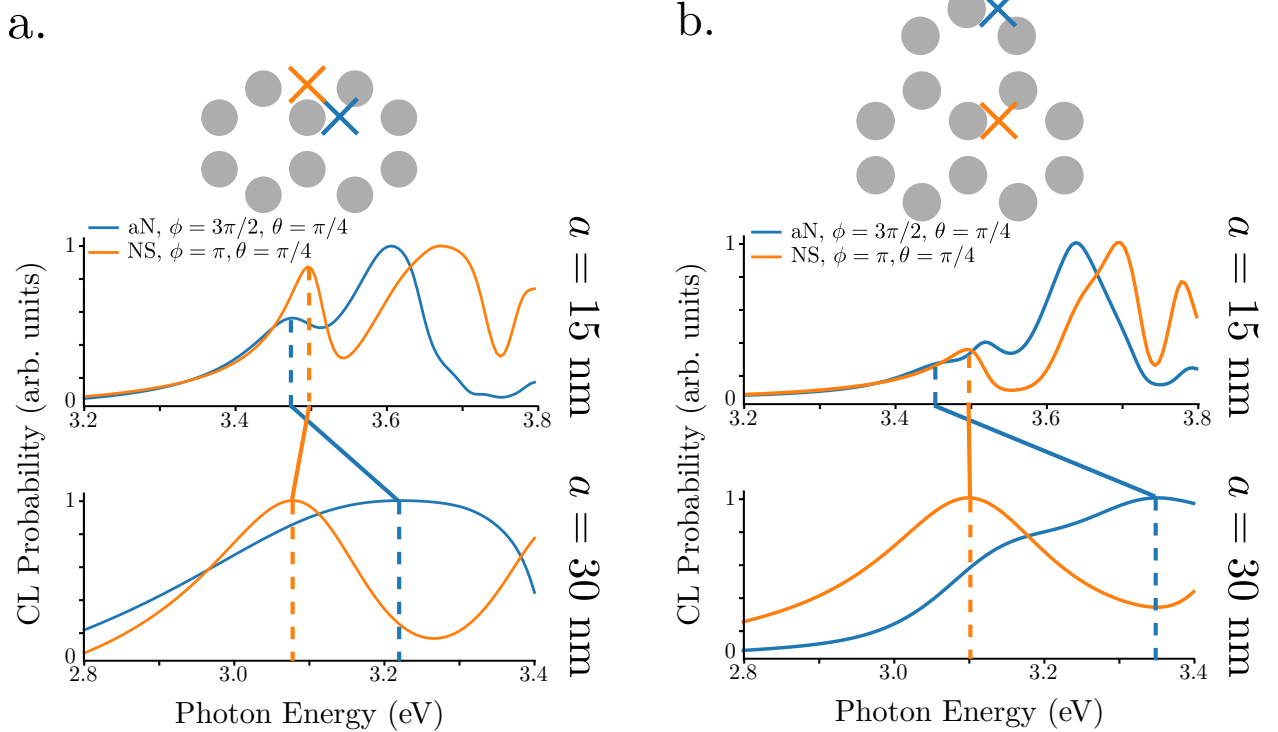

Figure 4: Angle-resolved cathodoluminescence spectra of the 2mer (a and b) and 3mer (c and d). By choosing the beam positions marked on the diagrams and choosing different angles at which to measure the light emitted, the magnetic modes of each oligomer can be disentangled. The colored "x's" correspond to colored traces. The blue traces show a collection angle of $\phi = 3\pi/2$ and the orange traces are for $\phi = \pi$, while both have $\theta = \pi/4$. Simulating these CL experiments with $r_0 = 15$ nm shows the aN modes lower in energy than the NS modes, as predicted. WIth $r_0 = 30$ nm, the modes switch, again as predicted.

In Figure 4 we show simulated point angle-resolved CL spectra of the 2-mer and 3-mer, with the electron beam position chosen so as to excite the aN (blue) and NS (orange) modes. Note however, due to the symmetry of the oligomers, the blue electron beam position excites not only the aN mode, but also weakly the NS mode. Since the radiation profile of the aN mode is orthogonal to that of the NS mode, it is possible to distinguish them by analyzing the angular distribution of emitted CL radiation. The ARCL spectra at two such angles are reported in Figure 4. These simulated spectra confirm the predictions of our model shown in Figure 2; specifically, between $a = 15 - 30$ nm, the aN and NS modes switch spectral order.

5 Magnetic Plasmon Resonance Frequencies and CL Spectra of Hexagonally-Packed Nanoclusters

Ref.[13] synthesizes and optically characterizes hexagonally-packed nanoclusters composed of noble metal nanoparticles in the intermediate size regime, between few particle oligomers and infinite arrays. Here, we apply our analytical modeling and numerical simulation to investigate the behavior of the magnetic plasmon resonances as a function of size, with an eye toward engineering magnetic resonances at particular resonance energies. Such tunability may be important in the design of future negative index materials with spectral tunability. Specifically, we consider hexagonally packed clusters composed of 13, 19, and 31 MNPs displayed in Figure 5 as well as the insets of Figure 6.

Figure 5 displays the signed magnetic field magnitude of two magnetic plasmon resonances of the 13-, 19-, and 31-particle hexagonally packed nanoclusters. The NS mode of each nanocluster is doubly degenerate as would be true of any structure with sixfold symmetry. In analogy to the previous oligomers, these magnetic modes are chosen because they are spectrally isolated from the other magnetic modes and because their radiation patterns are spatially orthogonal. The arrows denote the electric dipole moments on individual nanoparticles within the magnetic normal mode and the color denotes the strength of the magnetic

$|\boldsymbol{\mu}_{\text{tot}}| \neq 0 \ \ |\mathbf{d}_{\text{tot}}| = 0$ $|\boldsymbol{\mu}_{\text{tot}}| \neq 0 \ \ |\mathbf{d}_{\text{tot}}| = 0$ $|\boldsymbol{\mu}_{\text{tot}}| \neq 0 \ \ |\mathbf{d}_{\text{tot}}| = 0$

$|\mathbf{B}|$

$|\boldsymbol{\mu}_{\text{tot}}| = 0 \ \ |\mathbf{d}_{\text{tot}}| \neq 0$ $|\boldsymbol{\mu}_{\text{tot}}| = 0 \ \ |\mathbf{d}_{\text{tot}}| \neq 0$ $|\boldsymbol{\mu}_{\text{tot}}| = 0 \ \ |\mathbf{d}_{\text{tot}}| \neq 0$
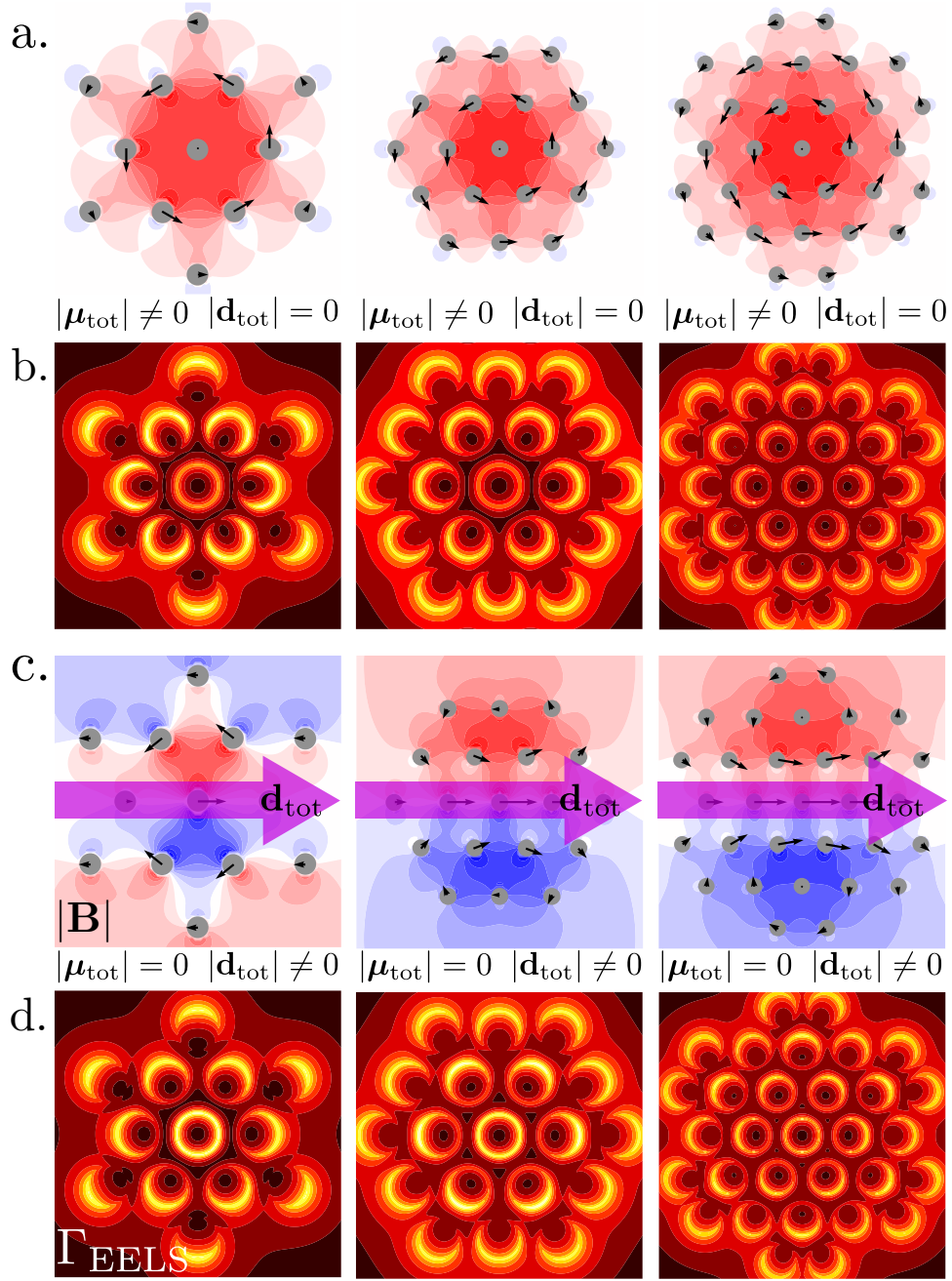
Γ_{EELS}

Figure 5: Signed magnetic field magnitudes of the modes of the 13-particle (a, b, and c), 19-particle (d, e, and f), and 31-particle (g, h, and i) clusters. Similarly to the 2mer and 3mer from before, we present only those magnetic modes with either NS and electric dipole character (a, b, d, e, g, and h) or with aN and magnetic dipole character (c, f, and i).

field. The net electric or magnetic dipole character of each magnetic resonance is denoted in the upper right hand corner of each panel.

Figure 6 displays the evolution of the aN and NS magnetic resonances with size, a. In contrast to the oligomers described previously, here the behavior of the nanocluster resonances with size is different due to the hexagonal packing as opposed to the open-ring structure of the oligomers. Nevertheless, the analytic model described previously is capable of predicting the magnetic spectrum. Most surprising is the behavior of the magnetic resonances of the 19- and 31-particle nanoclusters to oscillate with size as opposed to monotonically decrease in energy. Panels b, d, and f of Figure 6 display the relative strength of the near, intermediate, and far-field contributions to the electric dipole-electric dipole interaction energy and show that this oscillatory behavior is due specifically to retardation effects. This is contrary to intuition where increasing size causes monotonic redshifting. However this oscillatory behavior is not so unexpected; separating a MNP dimer causes its hybridized electric plasmon resonance frequencies to oscillate from bonding to anti-bonding and back.[20] In these nanoclusters, ARCL and patterns spectra provide a means to demonstrate this oscillation.

Figure 7 shows simulated ARCL spectra for the 13-, 19-, and 31-particle systems acquired at the two indicated beam positions and collection angles. Inspection of the EELS maps of the NS and aN magnetic resonances in rows b and d of Figure 5 indicates the optimal electron beam positions, that is, those positions with highest EEL probability, at which to excite each magnetic mode. As described previously, it is the electron beam selection rules and radiative profile of each mode help to identify the two magnetic resonances of interest. Because the aN mode radiates strongly in the xy-plane, and weakly in the z-direction, it is most easily detected at angles of $0 < \theta < \pi/2$. The NS mode is detected either for angles very close to the backward scattering direction ($\theta \approx 0$), or parallel to the impact plane (here, the y-direction for this particular beam position). The aN beam position also weakly excites the degenerate NS modes, meaning the corresponding CL spectrum will provide a secondary signature of the spectral location of that mode.
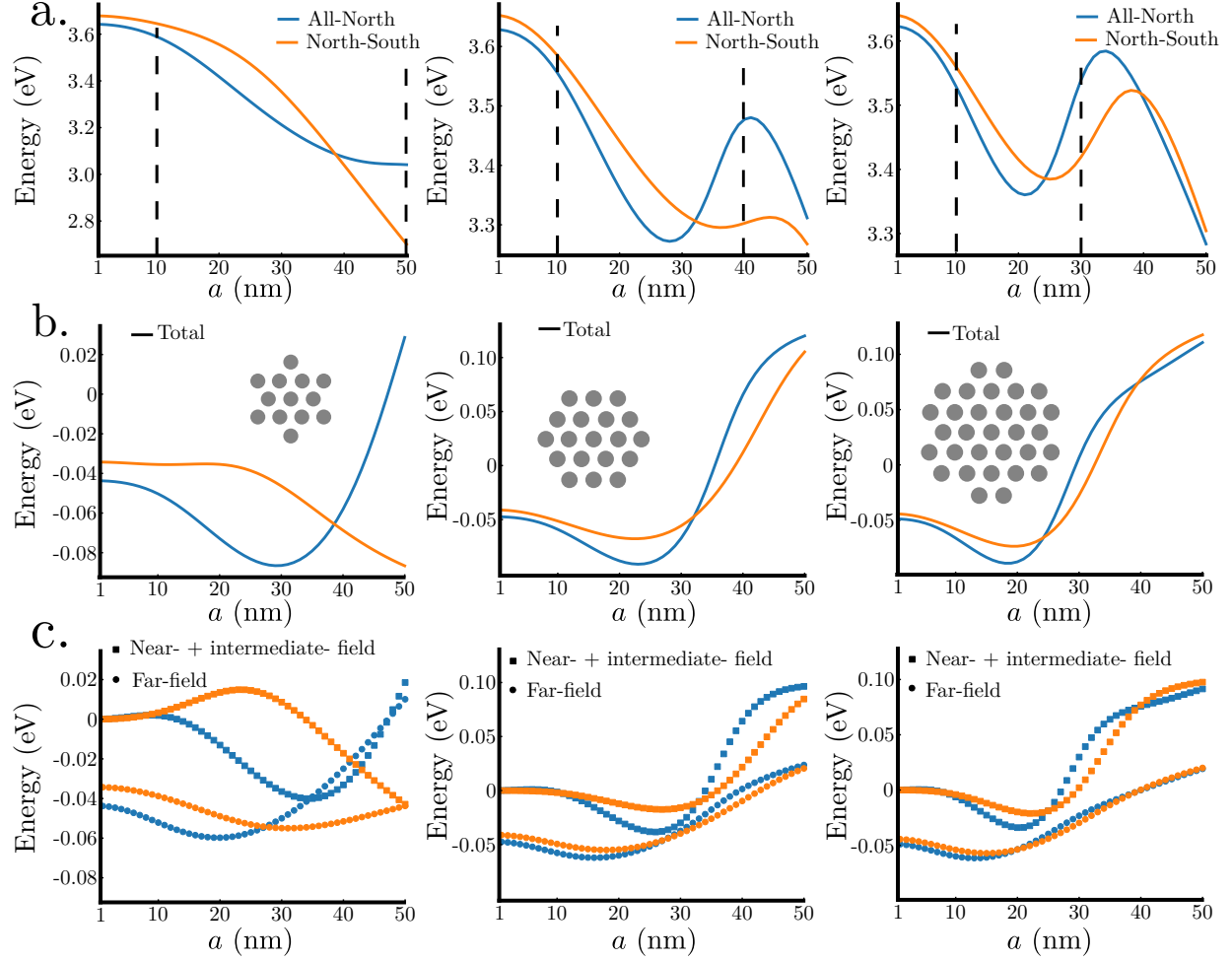
Figure 6: Eigenenergies and interaction energies for the magnetic modes of the 13- (a and b), 19- (c and d), and 31-particle (e and f) clusters. Unlike the previous 2mer and 3mer, at very small values of r_0, the aN modes are lower in energy than the NS modes. However, for each system a crossing point does occur between $r_0 = 30$ nm and $r_0 = 40$ nm. While the modes of the 13-particle system behave as expected, the aN and NS modes of the larger clusters behave contrary to the intuition built from the earlier model systems. At larger sizes, instead of a monotonic decrease in eigenenergies, the modes exhibit an increase in energy. Looking at the interaction energies, it becomes clear that this is again due to retardation effects, as the term that contributes the most anti-bonding character to the total interaction energy is the far-field. Furthermore, the 31-particle system exhibits a second crossing, unlike the other two structures, and the increase in its eigenenergies is maximized at smaller sizes.
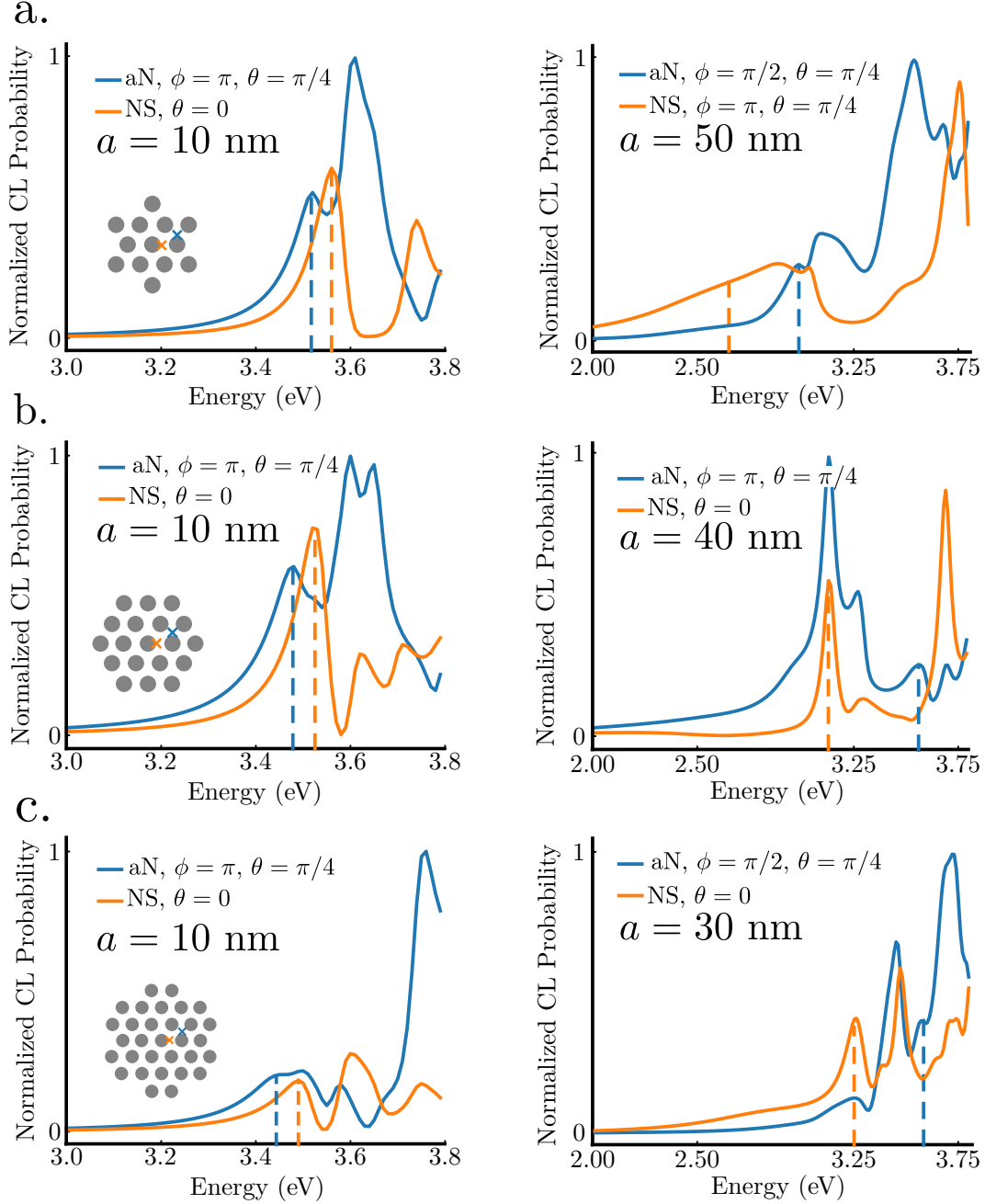
15

Figure 7: Simulated angle-resolved cathodoluminescence spectra of the 13-, 19-, and 31-particle systems. Blue spectra were acquired at the beam positions marked with a blue x in order to preferentially excite the aN mode. Orange spectra were collected at the points marked with an orange x in order to preferentially excite the x-polarized NS mode. Spectra for the 13-particle aggregate were computed for $r_0 = 10$ nm (a) and $r_0 = 50$ nm (b). Spectra for the 19-particle aggregate were computed for $r_0 = 10$ nm (c) and $r_0 = 40$ nm (d). Spectra for the 31-particle aggregate were computed for $r_0 = 10$ nm (e) and $r_0 = 30$ nm (f). The dashed lines in each spectrum indicate the peak location of the aN modes (blue curves) and the NS modes (orange curves). Each panel also displays the collection angles for each spectrum.

16

6   Conclusion

This paper is concluded.

7   Methods

Here we show how to derive the equations of motion describing magnetic plasmon resonances in nanoparticle clusters. References 10 and 43 describe how to map the solutions of Maxwell's Equations for electric plasmon resonances onto mechanical oscillators with effective masses. The resulting Hamiltonian for a system of N frictionless coupled oscillators is

$$H = \sum_i \frac{\mathbf{p}_i^2}{2m_{\mathrm{sp}}} + \frac{1}{2}m_{\mathrm{sp}}\omega_{\mathrm{sp}}^2\mathbf{q}_i^2 - \frac{e}{2}\sum_{ij,i\neq j}\mathbf{q}_i \cdot \mathbf{E}_j(\mathbf{r}_i), \tag{7}$$

where qi and $\mathbf{p}_i$ are the coordinate and momentum of each plasmon oscillator located at r_i with effective mass m_{sp} and resonance frequency ω_{sp}, defined previosuly; $\mathbf{E}_j(\mathbf{r}_i)$ is the full electric dipole field presented in Equation 2. The resulting equations of motion are,

$$\ddot{\mathbf{q}}_i = -\omega_{\mathrm{sp}}^2\mathbf{q}_i + \frac{e}{m_{\mathrm{sp}}}\sum_{j\neq i}\mathbf{E}_j(\mathbf{r}_i,\omega) \tag{8}$$

which is exactly Equation 1. From here, introducing time-dependence as a complex exponential, rewriting the electric field in terms of the plasmon coordinate, and performing a Fourier transform results in equations of motion in the frequency domain

$$(\omega_{\mathrm{sp}}^2 - \omega^2)\mathbf{q}_i - \frac{e^2}{m_{\mathrm{sp}}}\sum_{j\neq i}\mathbf{\Lambda}_{ij}(\omega) \cdot \mathbf{q}_j = 0. \tag{9}$$

It is this system of equations for the plasmon oscillator coordinates that we solve for the normal modes. Considering two identical, coupled, collinear oscillators as an example with dipole-dipole coupling strength $g_{12} =$ Equation 13 becomes

$$(\omega_{\text{sp}}^2 - \omega^2)q_1 - g_{12}(\omega)q_2 = 0 \tag{10}$$

and

$$(\omega_{\text{sp}}^2 - \omega^2)q_2 - g_{12}(\omega)q_1 = 0, \tag{11}$$

or equivalently

$$\begin{bmatrix} (\omega_{\text{sp}}^2 - \omega^2) & -g_{12}(\omega) \\ -g_{12}(\omega) & (\omega_{\text{sp}}^2 - \omega^2) \end{bmatrix} \begin{bmatrix} q_1 \\ q_2 \end{bmatrix} = \begin{bmatrix} 0 \\ 0 \end{bmatrix} \tag{12}$$

Solution of this system produces the hybridized resonance frequencies and normal modes. Finding the determinant of this matrix yields the eigenvalues of the collective modes,

$$\omega_{\pm} = \sqrt{\omega_{sp}^2 \pm g_{12}(\omega)}, \tag{13}$$

with corresponding normal mode coordinates

$$q_{\pm} = \frac{1}{\sqrt{2}}(q_1 \pm q_2) \tag{14}$$

Note that the coupling term $g_{12}(\omega)$ is frequency dependent, meaning the eigenvalue problem must be solved iteratively until convergence. The magnetic plasmon resonances and normal modes described herein are obtained as a straightforward extension of this example.

Acknowledgement

References

(1) Alù, A.; Salandrino, A.; Engheta, N. Negative effective permeability and left-handed materials at optical frequencies. *Opt. Express* **2006**, *14*, 1557–1567.

(2) Alù, A.; Engheta, N. Dynamical theory of artificial optical magnetism produced by rings of plasmonic nanoparticles. *Phys. Rev. B* **2008**, *78*, 085112.

(3) Hentschel, M.; Dregely, D.; Vogelgesang, R.; Giessen, H.; Liu, N. Plasmonic oligomers: The role of individual particles in collective behavior. *ACS Nano* **2011**, *5*, 2042–2050.

(4) Sheikholeslami, S. N.; García-Etxarri, A.; Dionne, J. A. Controlling the interplay of electric and magnetic modes via Fano-like plasmon resonances. *Nano Lett.* **2011**, *11*, 3927–3934.

(5) Qian, Z.; Hastings, S. P.; Li, C.; Edward, B.; McGinn, C. K.; Engheta, N.; Fakhraai, Z.; Park, S.-J. Raspberry-like metamolecules exhibiting strong magnetic resonances. *ACS Nano* **2015**, *9*, 1263–1270.

(6) Scholl, J. A.; García-Etxarri, A.; Aguirregabiria, G.; Esteban, R.; Narayan, T. C.; Koh, A. L.; Aizpurua, J.; Dionne, J. A. Evolution of plasmonic metamolecule modes in the quantum tunneling regime. *ACS Nano* **2016**, *10*, 1346–1354.

(7) Liu, H.; Genov, D. A.; Wu, D. M.; Liu, Y. M.; Steele, J. M.; Sun, C.; Zhu, S. N.; Zhang, X. Magnetic plasmon propagation along a chain of connected subwavelength resonators at infrared frequencies. *Phys. Rev. Lett.* **2006**, *97*, 243902.

(8) Liu, H.; Genov, D. A.; Wu, D. M.; Liu, Y. M.; Liu, Z. W.; Sun, C.; Zhu, S. N.; Zhang, X.

Magnetic plasmon hybridization and optical activity at optical frequencies in metallic nanostructures. *Phys. Rev. B* **2007**, *76*, 073101.

(9) Liu, N.; Mukherjee, S.; Bao, K.; Brown, L. V.; Dorfmüller, J.; Nordlander, P.; Halas, N. J. Magnetic plasmon formation and propagation in artificial aromatic molecules. *Nano Lett.* **2011**, *12*, 364–369.

(10) Liu, N.; Mukherjee, S.; Bao, K.; Li, Y.; Brown, L. V.; Nordlander, P.; Halas, N. J. Manipulating magnetic plasmon propagation in metallic nanocluster networks. *ACS Nano* **2012**, *6*, 5482–5488.

(11) Cherqui, C.; Bigelow, N. W.; Vaschillo, A.; Goldwyn, H.; Masiello, D. J. Combined tight-binding and numerical electrodynamics understanding of the STEM/EELS magneto-optical responses of aromatic plasmon-supporting metal oligomers. *ACS Photonics* **2014**, *1*, 1013–1024.

(12) Cherqui, C.; Wu, Y.; Li, G.; Quillin, S. C.; Busche, J. A.; Thakkar, N.; West, C. A.; Montoni, N. P.; Rack, P. D.; Camden, J. P. .; Masiello, D. J. STEM/EELS imaging of magnetic hybridization in symmetric and symmetry-broken plasmon oligomer dimers and all-magnetic fano interference. *Nano Lett.* **2016**, *16*, 6668–6676.

(13) Greybush, N. J.; Liberal, I. n.; Malassis, L.; Kikkawa, J. M.; Engheta, N.; Murray, C. B.; Kagan, C. R. Plasmon resonances in self-assembled two-dimensional Au nanocrystal metamolecules. *ACS Nano* **2017**, *11*, 2917–2927.

(14) Brandl, D. W.; Mirin, N. A.; Nordlander, P. Plasmon modes of nanosphere trimers and quadrumers. *J. Phys. Chem. B* **2006**, *110*, 12302–12310.

(15) Darvishzadeh-Varcheie, M.; Guclu, C.; Capolino, F. Magnetic nanoantennas made of plasmonic nanoclusters for photoinduced magnetic field enhancement. *Phys. Rev. Appl.* **2017**, *8*, 024033.

(16) Haynes, C. L.; McFarland, A. D.; Zhao, L.; Van Duyne, R. P.; Schatz, G. C.; Gun-narsson, L.; Prikulis, J.; Kasemo, B.; Käll, M. Nanoparticle optics: the importance of radiative dipole coupling in two-dimensional nanoparticle arrays. *J. Phys. Chem. B* **2003**, *107*, 7337–7342.

(17) Weick, G.; Woollacott, C.; Barnes, W. L.; Hess, O.; Mariani, E. Dirac-like plasmons in honeycomb lattices of metallic nanoparticles. *Phys. Rev. Lett.* **2013**, *110*, 106801.

(18) Turner, M. D.; Hossain, M. M.; Gu, M. The effects of retardation on plasmon hybridization within metallic nanostructures. *New J. Phys.* **2010**, *12*, 083062.

(19) Nordlander, P.; Oubre, C.; Prodan, E.; Li, K.; Stockman, M. I. Plasmon hybridization in nanoparticle dimers. *Nano Lett.* **2004**, *4*, 899–903.

(20) Dahmen, C.; Schmidt, B.; von Plessen, G. Radiation damping in metal nanoparticle pairs. *Nano Lett.* **2007**, *7*, 318–322.

(21) Clippe, P.; Evrard, R.; Lucas, A. A. Aggregation effect on the infrared absorption spectrum of small ionic crystals. *Phys. Rev. B* **1976**, *14*, 1715–1721.

(22) Aravind, P.; Nitzan, A.; Metiu, H. The interaction between electromagnetic resonances and its role in spectroscopic studies of molecules adsorbed on colloidal particles or metal spheres. *Surf. Sci.* **1981**, *110*, 189 – 204.

(23) Kottmann, J. P.; Martin, O. J. F. Retardation-induced plasmon resonances in coupled nanoparticles. *Opt. Lett.* **2001**, 1096–1098.

(24) Prodan, E.; Radloff, C.; Halas, N. J.; Nordlander, P. A hybridization model for the plasmon response of complex nanostructures. *Science* **2003**, *302*, 419–422.

(25) Prodan, E.; Nordlander, P. Plasmon hybridization in spherical nanoparticles. *J. of Chem. Phys.* **2004**, *120*, 5444–5454.

(26) Rechberger, W.; Hohenau, A.; Leitner, A.; Krenn, J.; Lamprecht, B.; Aussenegg, F. Optical properties of two interacting gold nanoparticles. *Opt. Commun.* **2003**, *220*, 137 – 141.

(27) Bouhelier, A.; Bachelot, R.; Im, J. S.; Wiederrecht, G. P.; Lerondel, G.; Kostcheev, S.; Royer, P. Electromagnetic interactions in plasmonic nanoparticle arrays. *J. Phys. Chem. B* **2005**, *109*, 3195–3198.

(28) Myroshnychenko, V.; Rodriguez-Fernandez, J.; Pastoriza-Santos, I.; Funston, A. M.; Novo, C.; Mulvaney, P.; Liz-Marzan, L. M.; Garcia de Abajo, F. J. Modelling the optical response of gold nanoparticles. *Chem. Soc. Rev.* **2008**, *37*, 1792–1805.

(29) Davis, T. J.; Vernon, K. C.; Gómez, D. E. Designing plasmonic systems using optical coupling between nanoparticles. *Phys. Rev. B* **2009**, *79*, 155423.

(30) Kinnan, M. K.; Chumanov, G. Plasmon coupling in two-dimensional arrays of silver nanoparticles: II. Effect of the particle size and interparticle distance. *J. Phys. Chem. C* **2010**, *114*, 7496–7501.

(31) Kravets, V. V.; Pinchuk, A. O. Near-, middle-, and far-field dipolar interactions in gold nanoparticle arrays. *Proc. SPIE* **2016**, *9724*, 97240B–97240B–8.

(32) Hohenester, U. Simulating electron energy loss spectroscopy with the MNPBEM toolbox. *Comp. Phys. Comm.* **2014**, *185*, 1177 – 1187.

(33) Coenen, T.; Vesseur, E. J. R.; Polman, A.; Koenderink, A. F. Directional emission from plasmonic YagiâĂŞUda antennas probed by angle-resolved cathodoluminescence spectroscopy. *Nano Lett.* **2011**, *11*, 3779–3784.

(34) Coenen, T.; Vesseur, E. J. R.; Polman, A. Angle-resolved cathodoluminescence spectroscopy. *Appl. Phys. Lett.* **2011**, *99*, 143103.

(35) Coenen, T.; Bernal Arango, F.; Femius Koenderink, A.; Polman, A. Directional emission from a single plasmonic scatterer. *Nat. Comm.* **2014**, *5*, 3250.

(36) Pendry, J. B. Focus issue: negative refraction and metamaterials. *Opt. Express* **2003**, *11*, 639–639.

(37) Fang, N.; Lee, H.; Sun, C.; Zhang, X. Sub-diffraction-limited optical imaging with a silver superlens. *Science* **2005**, *308*, 534–537.

(38) Cai, W.; Chettiar, U. K.; Kildishev, A. V.; Shalaev, V. M. Optical cloaking with metamaterials. *Nature Photonics* **2007**, *1*, 224.

(39) Pinchuk, A. O.; Schatz, G. C. Metamaterials with gradient negative index of refraction. *J. Opt. Soc. Am. A* **2007**, *24*, A39–A44.

(40) Shalaev, V. M. Transforming light. *Science* **2008**, *322*, 376–379.

(41) Valentine, J.; Zhang, S.; Zentgraf, T.; Ulin-Avila, E.; Genov, D. A.; Bartal, G.; Zhang, X. Three-dimensional optical metamaterial with a negative refractive index. *Nature* **2008**, *455*, 376–379.

(42) Ferrari, J. A.; Perciante, C. D. Superlenses, metamaterials, and negative refraction. *J. Opt. Soc. Am. A* **2009**, *26*, 78–84.

(43) Cherqui, C.; Thakkar, N.; Li, G.; Camden, J. P.; Masiello, D. J. Characterizing localized surface plasmons using electron energy-loss spectroscopy. *Ann. Rev. Phys. Chem.* **2016**, *67*, 331–357.

(44) Purcell, E. M.; Pennypacker, C. R. Scattering and absorption of light by nonspherical dielectric grains. *Astrophys. J.* **1973**, *186*, 705–714.

(45) Hohenester, U.; Trügler, A. MNPBEM - A matlab toolbox for the simulation of plasmonic nanoparticles. *Comp. Phys. Comm.* **2012**, *183*, 370 – 381.

(46) Jain, P. K.; El-Sayed, M. A. Noble metal nanoparticle pairs: effect of medium for enhanced nanosensing. *Nano Lett.* **2008**, *8*, 4347–4352.

(47) Jackson, J. D. *Classical Electrodynamics*, 3rd ed.; Wiley: New York, NY, 1999.

(48) Schwinger, J.; Deraad, L.; Milton, K.; Tsai, W.; Norton, J. *Classical Electrodynamics*; Advanced book program; Avalon Publishing, 1998.

(49) Liu, W.; Miroshnichenko, A. E.; Neshev, D. N.; Kivshar, Y. S. Broadband unidirectional scattering by magneto-electric core-shell nanoparticles. *ACS Nano* **2012**, *6*, 5489–5497.

(50) Asenjo-Garcia, A.; García de Abajo, F. J. Plasmon electron energy-gain spectroscopy. *New J. Phys.* **2013**, *15*, 103021.

Graphical TOC Entry